Electrical generation and detection of spin waves in a quantum Hall ferromagnet

Wei, Di S.; Van Der Sar, Toeno; Lee, Seung Hwan; Watanabe, Kenji; Taniguchi, Takashi; Halperin, Bertrand I.; Yacoby, Amir

DOI
10.1126/science.aar4061

Publication date
2018

Document Version
Final published version

Published in
Science

Citation (APA)
Wei, D. S., Van Der Sar, T., Lee, S. H., Watanabe, K., Taniguchi, T., Halperin, B. I., & Yacoby, A. (2018). Electrical generation and detection of spin waves in a quantum Hall ferromagnet. *Science*, *362*(6411), 229-233. https://doi.org/10.1126/science.aar4061

MAGNETISM

Electrical generation and detection of spin waves in a quantum Hall ferromagnet

Di S. Wei[1], Toeno van der Sar[2]*, Seung Hwan Lee[2], Kenji Watanabe[3], Takashi Taniguchi[3], Bertrand I. Halperin[2], Amir Yacoby[1,2]†

Spin waves are collective excitations of magnetic systems. An attractive setting for studying long-lived spin-wave physics is the quantum Hall (QH) ferromagnet, which forms spontaneously in clean two-dimensional electron systems at low temperature and in a perpendicular magnetic field. We used out-of-equilibrium occupation of QH edge channels in graphene to excite and detect spin waves in magnetically ordered QH states. Our experiments provide direct evidence for long-distance spin-wave propagation through different ferromagnetic phases in the *N* = 0 Landau level, as well as across the insulating canted antiferromagnetic phase. Our results will enable experimental investigation of the fundamental magnetic properties of these exotic two-dimensional electron systems.

Quantum Hall (QH) ferromagnetism arises from the interaction of electrons in massively degenerate, quantized energy levels known as Landau levels (LLs) (*1*). When disorder is low enough for Coulomb interactions to manifest, the electrons in partially filled LLs spin-polarize spontaneously to minimize their exchange energy, with the single-particle Zeeman effect dictating their polarization axis (*2*, *3*). In graphene, these phenomena give rise to ferromagnetic phases when the $N = 0$ LL is at one-quarter and three-quarters filling (*4*–*8*). Such QH ferromagnets have an insulating topological bulk and spin-polarized edge states. Furthermore, a canted antiferromagnetic (CAF) state is believed to emerge at one-half filling, with a canting angle determined by the competing valley anisotropy and Zeeman energy (*9*, *10*). Spin waves, also known as magnons, are the lowest-energy excitation in both the QH ferromagnet and the CAF state (*1*, *11*, *12*) and could provide crucial information about these topologically nontrivial magnetic states.

In our experimental setup, we generate magnons by creating an imbalance of chemical potential between two edge states of opposite spin that run along the boundary of a QH magnet. If this imbalance is smaller than the energy required for generating magnons in the QH magnet (and there are no thermal magnons already present in the system), scattering between these two edge states is forbidden because the change in angular momentum of a scattered electron cannot be absorbed by the system. Indeed, previous measurements have shown that oppositely spin-polarized edge channels do not equilibrate as long as the imbalance is small (*13*, *14*). However, we find that edge-channel equilibration commences when the imbalance exceeds the minimum energy required for exciting magnons in the QH ferromagnet. Because the magnetization of the QH ferromagnet is extremely dilute, there are negligible demagnetizing fields and the minimum energy to excite magnons is given by the Zeeman energy $E_Z = g\mu_B B$ (*1*, *15*), where g is the electron g-factor, μ_B is the Bohr magneton, and B is the external magnetic field. Although magnon generation does not directly affect the conductance of the system, the reverse process of magnon absorption by faraway edge states does, allowing us to detect the propagation of magnons electrically, in close analogy to the conventional detection of magnons in insulators via the inverse spin Hall effect (*16*–*19*).

To demonstrate spin-wave propagation, we begin with a dual-gated monolayer graphene device (device 1) where the central region can be tuned to a filling factor different from that of the adjacent regions (Fig. 1A). Connecting the two leads is a chiral edge state that carries spin-polarized electrons aligned with the magnetic

[1]John A. Paulson School of Engineering and Applied Sciences, Harvard University, Cambridge, MA 02138, USA. [2]Department of Physics, Harvard University, Cambridge, MA 02138, USA. [3]National Institute for Materials Science, Tsukuba, Ibaraki 305-0044, Japan.
*Present address: Kavli Institute of Nanoscience, Delft University of Technology, 2628CJ Delft, Netherlands.
†Corresponding author. Email: yacoby@physics.harvard.edu

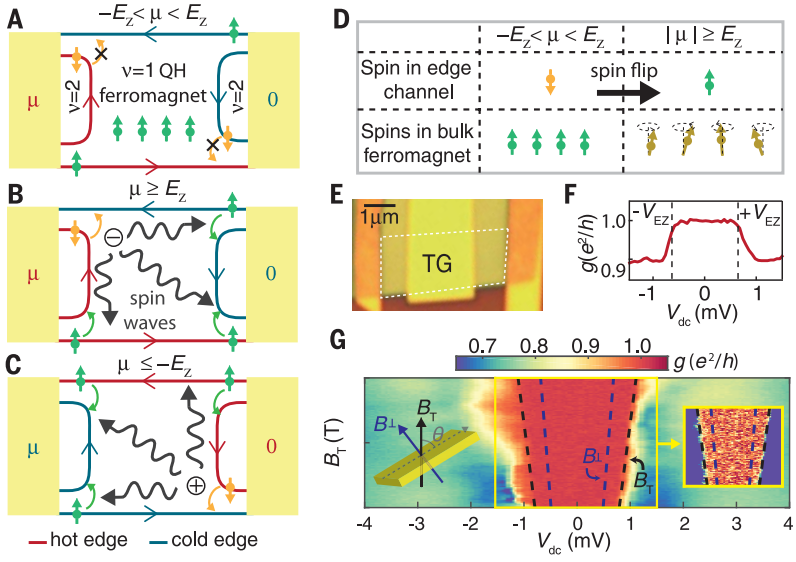

Fig. 1. Magnons in a quantum Hall ferromagnet. (**A** to **C**) A chemical potential difference (μ) is applied between the left and right leads. Edge channels with high and low chemical potential are labeled "hot" and "cold," respectively. Spin-up and spin-down polarization are denoted by the green and orange arrows, respectively. The central region is tuned to ν = 1 and adjacent regions are tuned to ν = 2. (A) The chemical potential difference between the spin-up and spin-down edge channel is less than the Zeeman energy (E_Z), and scattering is suppressed. (B) $\mu \geq E_Z$: Electrons have enough energy to flip their spins and transfer spin angular momentum (magnons) into the bulk (at the encircled minus sign). These magnons are absorbed at distant corners, causing electrons to flip from spin-up into spin-down channels. (C) $\mu \leq -E_Z$: Magnons are generated at the location denoted by the encircled plus sign. (**D**) Bulk spin polarization before and after magnon creation, conserving total spin angular momentum. (**E**) Optical micrograph of device 1; graphene is outlined in white. TG, top gate. (**F**) A dc voltage (V_{dc}) and a 50-μV ac excitation voltage (V_{ac}) are applied to the left contact, and the differential conductance (dI/dV, where $V = V_{ac} + V_{dc}$) is measured through the right contact ($B_\perp = 4$ T, $V_{TG} = -0.18$ V, $V_{BG} = 3$ V). Conductance is quantized to e^2/h until $|\mu| \geq E_Z$. (**G**) dI/dV as a function of bias and magnetic field. The blue dashed line is the Zeeman energy $E_{Z\perp} = g\mu_B B_\perp$ calculated using the perpendicular magnetic field $B_\perp$; the black dashed line is the Zeeman energy $E_{ZT} = g\mu_B B_T$ calculated using the total field B_T. Both the top gate (V_{TG}) and the back gate (V_{BG}) are swept to stay at ν = 1 throughout the device from 7 T ($V_{TG} = 0.16$ V, $V_{BG} = 0.73$ V) to 5 T ($V_{TG} = 0.12$ V, $V_{BG} = 0.44$ V). The decrease in conductance from e^2/h evolves linearly with the magnetic field, coinciding with E_{ZT} rather than $E_{Z\perp}$. Left inset: The sample is fixed at a 45° angle to $B_\perp$. Right inset: A saturated color plot (from 0.98 to 1.02 e^2/h) of the region enclosed by the yellow box. All measurements are conducted in a cryostat with a base temperature of 20 mK.

field, which we call spin-up. We tune the central region to a three-quarters filled LL (ν = 1), whereas the outer regions are tuned to a nonmagnetic fully filled LL (ν = 2). We apply a source-drain voltage V_{dc} to induce a difference in chemical potential $\mu = -eV_{dc}$ between the edge channels emerging from the two contacts, where e is the electron charge. Once $|\mu| \geq E_Z$, an electron traveling in a high-energy ("hot") spin-down edge state can relax into a low-energy ("cold") spin-up edge state by emitting a magnon into the ferromagnetic bulk (Fig. 1, B and C). Because equilibration must occur close to the ferromagnetic bulk in order to launch magnons, the edge states must equilibrate over short length scales at localized "hot spots" where the hot and cold edges meet. This makes graphene an ideal platform to observe this phenomenon, because edge state equilibration in graphene can occur over length scales of <1 μm (*13*, *20*, *21*) [see (*22*) for further discussion]. Because only spin-down angular momentum can be propagated into the spin-up bulk, magnon generation occurs at the location denoted by an encircled minus sign when $\mu \geq E_Z$ (Fig. 1B) and at the location denoted by an encircled plus sign when $\mu \leq -E_Z$ (Fig. 1C). These magnons propagate through the insulating QH ferromagnet and can be absorbed by the reverse process between other edge channels (Fig. 1, B and C), which causes a deviation in the conductance from a well-quantized ν = 1 QH state.

When we measure the conductance of the graphene device (Fig. 1E; atomic force microscopy image in fig. S3) as a function of V_{dc}, we find that the ν = 1 QH ferromagnet remains precisely quantized at the expected value of e^2/h, and then changes once the applied bias reaches the Zeeman threshold ($V_{dc} = \pm V_{EZ} = \mp E_Z/e$), as expected from our model (Fig. 1F). Interestingly, we find that thanks to contact doping (*22*, *23*) we can tune the entire device to ν = 1 and find the same phenomenon of conductance deviation at the Zeeman threshold (*22*) (fig. S4).

By tilting the external magnetic field with respect to the sample-plane normal axis, we verify that the change in conductance occurs when the applied chemical potential exceeds the bare Zeeman energy $E_Z = g\mu_B B_T$ ($g = 2$), which is given by the total field B_T (Fig. 1G; sample is tuned entirely to ν = 1). In contrast, previous transport studies of spin and valley excitations in graphene and GaAs have only found excitations related to the exchange energy gap (*2*, *3*, *24*), which depends on the component of the field perpendicular to the sample plane ($B_\perp$). Our tilted-field measurements therefore corroborate our magnon-based interpretation of the observed change in sample conductance. All further experiments described in this work are done at perpendicular field.

The conductance change at E_Z can either be positive or negative, depending on the number of magnons absorbed at each contact. To examine this, we use different sets of leads in the same device (Fig. 2A, device 2) to perform two-terminal conductance measurements. We start with leads L_2 and L_1 in Fig. 2B. We label the amount of redistributed chemical potential at each of the absorption sites ε_i, with i indexing the absorption site (note that $\varepsilon_i = 0$ for $-E_Z < \mu < +E_Z$), where ε_i is proportional to the number of magnons absorbed at site i. Absorption at ε_1 and absorption at ε_2 have opposite effects on the conductance, as magnon absorption transfers chemical potential from the outer edge to the inner edge. Therefore, for $\mu \geq E_Z$, magnon absorption at ε_1 decreases the particle current ($I_P = -I/e$, where I is the charge current), whereas magnon absorption at ε_2 increases I_P (Fig. 2B). For $\mu \leq -E_Z$, the hot and cold reservoirs are reversed, and we now consider the change to the negative particle current $-I_P$. Although ε_1 still decreases the particle current, I_P is now negative, and so ε_1 actually increases the magnitude of the particle current ($|-I_P|$); similarly, for $\mu \leq -E_Z$, ε_2 decreases $|-I_P|$ (Fig. 2C). We can quantify this using current conservation to formulate the differential conductance as a function of ε_i and μ:

$$\frac{dI}{dV} = \frac{dI_P}{d\mu} = \frac{1}{R_Q}\left(1 + \frac{d\varepsilon_2}{d\mu} - \frac{d\varepsilon_1}{d\mu}\right) \quad (1)$$

where $R_Q = h/e^2$ is the resistance quantum, $V = V_{ac} + V_{dc}$, and we neglect contact resistance [see (*22*) for a derivation that takes contact resistance into account]. We find that the conductance decreases at negative bias and increases at positive bias (Fig. 2D), indicating that $\varepsilon_1 > \varepsilon_2$ for both positive and negative bias. This implies that more magnons are absorbed at ε_1 than at ε_2. Because our contacts have all been fabricated identically, we conclude that this is because ε_1 is closer to magnon generation than ε_2 (for both positive and negative bias; Fig. 2, A and B). Using different sets

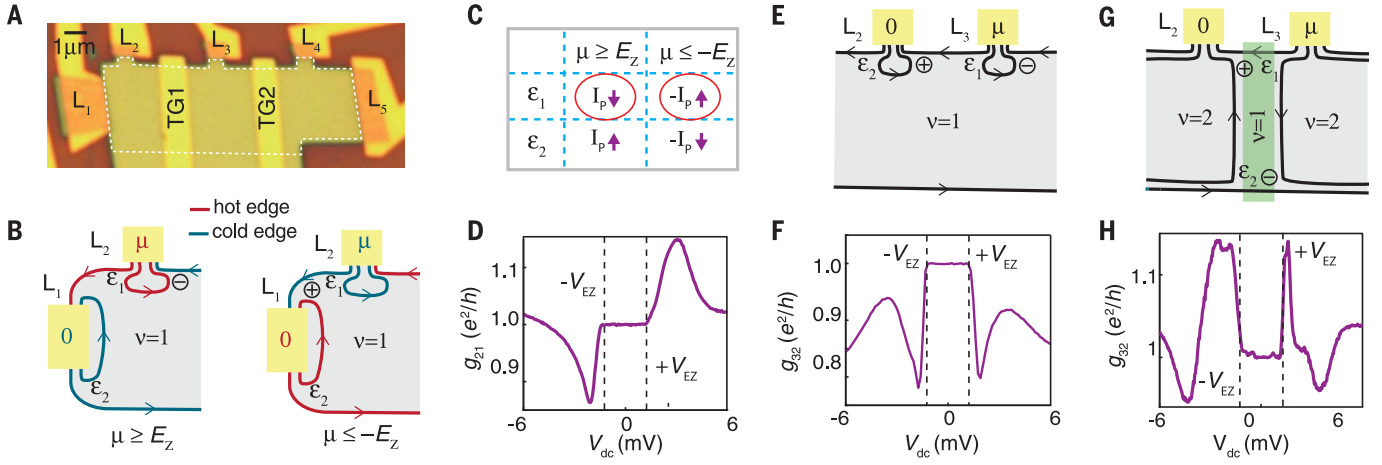

Fig. 2. Effects of relative magnon absorption on conductance. (**A**) Optical micrograph of device 2. Graphene is outlined in white. (**B**) Schematic of a two-terminal conductance measurement using leads L_2 and L_1 where hot and cold edges are colored red and blue, respectively, for both $\mu \geq E_Z$ (left) and $\mu \leq -E_Z$ (right), and the magnon generation site is labeled by the encircled plus or minus sign indicating positive or negative bias. $\mu \geq E_Z$: Magnon absorption at ε_1 transfers chemical potential from a forward-moving edge to a backward-moving edge, causing the particle current ($I_P = -I/e$) to decrease. Conversely, magnon absorption at ε_2 transfers chemical potential from a backward-moving edge to a forward-moving edge, increasing I_P. $\mu \leq -E_Z$: Magnon absorption at ε_1 causes an increase in $|-I_P|$; absorption at ε_2 causes a decrease in $|-I_P|$. (**C**) The effects of ε_1 and ε_2 at $\mu \geq E_Z$ and $\mu \leq -E_Z$. The current changes caused by ε_1 are dominant and are circled in red. The purple arrows indicate an increase (up) or decrease (down) in the magnitude of the signed particle current. (**D**) Conductance from L_2 to L_1 ($g_{21} = dI/dV = dI_P/d\mu$) decreases at $V_{dc} = -V_{EZ}$ and increases at $V_{dc} = V_{EZ}$, indicating that ε_1 has a larger effect than ε_2 ($B = 8$ T, $V_{BG} = 4$ V). See (*22*) for full circuit analysis. (**E** and **F**) Conductance from L_3 to L_2 (g_{32}) where the entire device is tuned to ν = 1 ($V_{BG} = 4$ V; TG1 = 0 V is not shown). At positive bias, $\varepsilon_2 > \varepsilon_1$, and at negative bias, $\varepsilon_1 > \varepsilon_2$, resulting in a conductance drop for both biases. (**G** and **H**) Conductance from L_3 to L_2 (g_{32}) where TG1 is tuned to $\nu_{TG1} = 1$ (TG1 = −0.36 V), whereas the regions outside are set to $\nu_{BG} = 2$ ($V_{BG} = 6.5$ V). At positive bias, $\varepsilon_1 > \varepsilon_2$, and at negative bias, $\varepsilon_2 > \varepsilon_1$, resulting in a conductance rise for both biases. See fig. S5 for a detailed analysis.

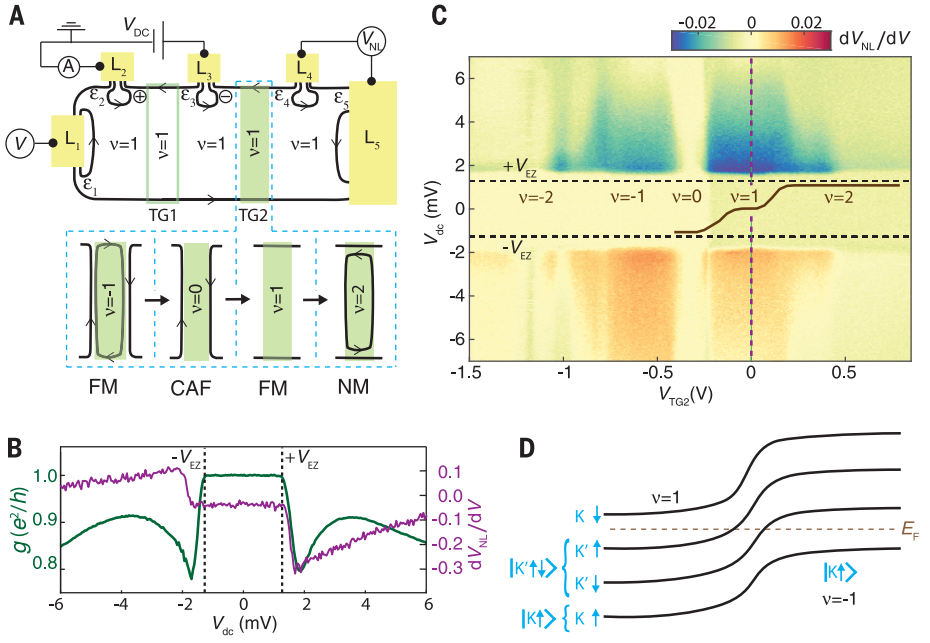

Fig. 3. Nonlocal voltage signal due to magnon absorption. Shown are the data from device 2. (**A**) Schematic circuit configuration for measuring a nonlocal voltage in device 2. The filling factor under TG1 (ν_{TG1}) is 1 for all measurements, whereas the filling factor under TG2 (ν_{TG2}) is swept from −2 to 2, and the rest of the device is kept at ν_{BG} = 1 (V_{BG} = 4 V). The bottom panel highlights the magnetic properties of different cases of ν_{TG2}: nonmagnetic (NM), ferromagnetic (FM), or canted antiferromagnetic (CAF). (**B**) S_{NL} (purple) superimposed onto d*I*/d*V* (green) as a function of V_{dc} when ν_{TG2} = 1 (B = 8 T). The onset of S_{NL} is slightly offset from the decrease in conductance, indicating that magnon generation needs to reach a threshold before being absorbed in distant contacts. (**C**) A pronounced S_{NL} signal when ν_{TG2} = 1 and ν_{TG2} = −1 (see fig. S8 for similar measurements using TG1). Tuning TG2 to the nonmagnetic QH phases (ν_{TG2} = 2 and ν_{TG2} = −2), as well as the ν_{TG2} = 0 CAF state, strongly suppresses S_{NL}. There is a small finite background S_{NL} when edge states pass through TG2, discussed in fig. S7B. Solid brown curve indicates where ν_{TG2} = 0, 1, and 2 (fig. S7, C and D). (**D**) The spatial variation of the LLs at a ν = 1 / ν = −1 junction, with the expected valley and spin polarizations of each level labeled.

of contacts and top gates (Fig. 2, E to H), we can change the relative distances of ε_i to the locations of magnon generation. We confirm that for each configuration, the conductance values after E_Z correspond to a greater number of magnons absorbed at the site closer to magnon generation.

This change to the conductance is not a consequence of QH breakdown. Conductance deviations after the Zeeman threshold that depend on the sign of V_{dc} are not explained by any current breakdown theories (*25*). Additionally, we find that the threshold voltage bias does not depend on the lead configuration (Fig. 2), the size of the ν = 1 region (fig. S4), or the density of the ν = 1 region (fig. S6). All of these observations are inconsistent with trivial QH breakdown but are consistent with our magnon model. In total, we have measured this ν = 1 conductance deviation occurring at the Zeeman energy for eight devices of widely varying geometries (figs. S3, S4, and S11).

Thus far, we have established that we are able to generate and absorb magnons at current carrying contacts. If these chargeless excitations propagate through the insulating bulk, we also expect to see signatures of magnon propagation and absorption via nonlocal voltage measurements (dV_{NL}/dV, referred to as the nonlocal signal S_{NL}), away from the source-drain current. To measure S_{NL}, we use L_3 and L_2 in device 2 as source-drain contacts, and use contacts L_4 and L_5 as voltage probes (Fig. 3A). These contacts are separated from the source-drain contacts by a top gate (TG2), which we tune between ν_{TG2} = −2 and ν_{TG2} = 2, whereas all other regions are tuned to ν = 1. The conductance g between L_3 and L_2 drops at $\pm V_{EZ}$ in accordance with our model (Fig. 3B), whereas magnon generation is largely unaffected by TG2 (fig. S7A). At ν_{TG2} = 1, we measure a change in S_{NL} at $\pm V_{EZ}$ owing to the relative absorption at each magnon absorption site (ε_i).

The sign of S_{NL} indicates that there is more magnon absorption at sites closer to where magnon generation occurs. Through current conservation (*22*), we find that the measured differential voltage (unitless) is

$$\frac{dV_{NL}}{dV} = \left(\frac{d\varepsilon_4}{d\mu} - \frac{d\varepsilon_5}{d\mu}\right) \quad (2)$$

The site labeled by ε_4 is closer to magnon generation than ε_5 for both negative and positive bias, so $d\varepsilon_4 > d\varepsilon_5$. However, the differential change in voltage ($d\varepsilon_i/d\mu$) is negative for $V_{dc} \geq V_{EZ}$ and positive for $V_{dc} \leq -V_{EZ}$, corresponding to an overall negative value for S_{NL} at $V_{dc} \geq V_{EZ}$ and a positive value at $V_{dc} \leq -V_{EZ}$ (Fig. 3C).

The device geometry used for our nonlocal measurements allows us to tune TG2 away from ν_{TG2} = 1, and thereby examine magnon transmission through different filling factors. We observe that when ν_{TG2} = −1, the signal S_{NL} is almost identical to when ν_{TG2} = 1 (Fig. 3C and fig. S8). This signal arises in the absence of any charge leakage across the ν_{TG2} = −1 region (fig. S9), so that changes in S_{NL} can be attributed to magnon transport through the ν_{TG2} = −1 ferromagnet. This suggests that there is neither spin nor valley mismatch between the ferromagnetic states on either side of the boundary. We therefore propose an ordering of the LLs that does not require a spin or valley flip for magnons to travel across the interface between ν_{BG} = 1 and ν_{TG2} = −1 [Fig. 3D; see (*22*) for a theoretical discussion].

In addition, we unexpectedly find that S_{NL} is suppressed at $\pm V_{EZ}$ when ν_{TG2} = 0. For nonmagnetic regions such as ν_{TG2} = 2, it is expected that magnons will be blocked from passing through, as experimentally confirmed in Fig. 3C (the nonlocal signal occurring at the transition between ν = 1 and ν = 2 is explained in fig. S7E). However, ν = 0 is purportedly a CAF, which is theoretically capable of hosting even zero-energy magnons (*12*). It appears that the probability for an incident magnon to be transmitted across the junction between the ν = 0 and ν = 1 regions is very small for energies close to E_Z. This may be caused by, in part, the mismatch in propagation velocities in the two phases, or a barrier due to the complex nature of the interface region. Close to the boundary with a ν = 1 phase, the ground state of the ν = 0 phase may not have canted spins but may instead be in an aligned antiferromagnet state, where spins are parallel to the magnetic field on one sublattice and antiparallel on the other. Eventually, far from the boundary, we may expect the local spin arrangement to rotate into the CAF orientation (Fig. 4B). In the transition region, the minimum magnon energy will be larger than E_Z, thanks to effects of the valley-dependent interaction terms (*10*), which were initially responsible for the antiferromagnet arrangement to be favored over the ferromagnetic arrangement. To cross from the ν = 1 region to the CAF region, a magnon with energy close to E_Z would have to tunnel through the barrier region, and we would expect the transmission rate to be low. If the magnons have enough energy to overcome this barrier, they should be able to more easily enter the CAF region. Figure 4C shows that we can experimentally exceed this barrier, where we see nonlocal signals at higher $|V_{dc}|$ with signs in agreement with our magnon model. The onset of this magnon

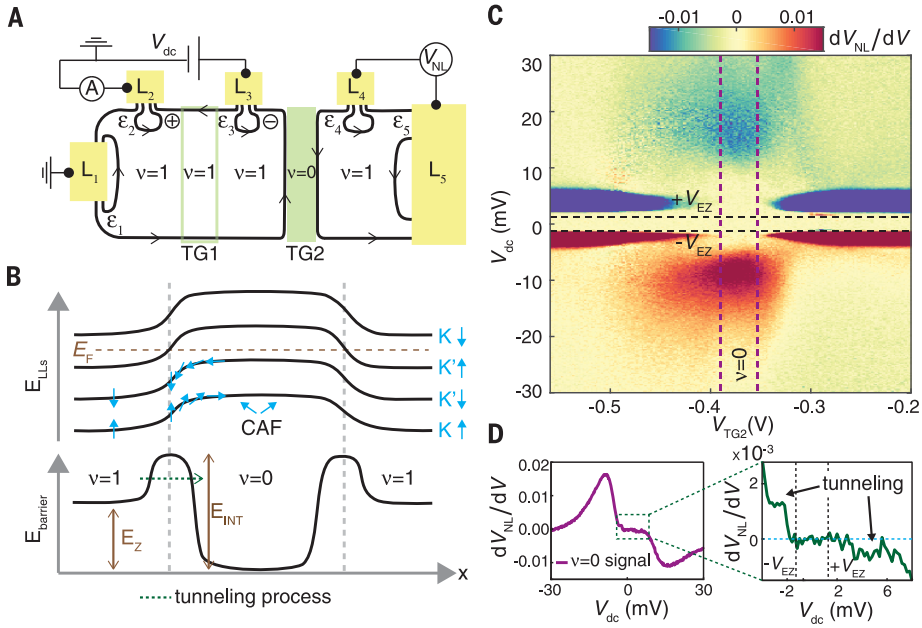

Fig. 4. Nonlocal voltage signal caused by magnon propagation through the ν = 0 CAF. (**A**) Schematic of the circuit used to measure S_{NL} in device 2 across a ν = 0 region; ν_{TG1} = 1 for all measurements, whereas ν_{TG2} is swept from −1 to 1 (ν_{BG} = 1, V_{BG} = 4 V). (**B**) Top: Postulated spatial variation of the LLs and spin arrangement in a ν = 1, ν = 0, ν = 1 geometry. Close to the interface between ν = 1 and ν = 0, spins in the two filled LLs prefer to be in an aligned antiferromagnetic (AF) arrangement. Deeper in the ν = 0 region, the spins rotate into the CAF phase. Because the minimum magnon energy in the aligned AF region is higher than E_Z, it should present a barrier for incident magnons close to the energy threshold. Bottom: Energy barrier seen by the magnons as a function of position, where E_{INT} is the energy barrier of the interface. (**C**) When magnons are generated, we see another onset of S_{NL} at energies exceeding $\pm V_{EZ}$ (B = 8 T), indicating that higher-energy magnons have overcome E_{INT} and have propagated through the ν = 0 region underneath TG2. Purple dashed lines indicate a region where vertical line cuts were taken and averaged to obtain the line trace in (D). (**D**) A clear onset of S_{NL} is shown at biases exceeding $\pm V_{EZ}$ when ν_{TG2} = 0. It is not currently understood why the signal is asymmetric in both energy of onset and strength of signal. The zoomed-in region shows a clear increase in S_{NL} at $-V_{EZ}$ and a signal consistent with a decrease, slightly offset from $+V_{EZ}$, indicating that magnons can tunnel through the interface barrier at lower energies (S_{NL} is offset by 0.01 μV at V_{dc} = 0 and is manually corrected for).

signal is unaffected by any charge transport across the ν_{TG2} = 0 region (fig. S10). Closely examining the signal at ν_{TG2} = 0, we see signals commencing at $\pm V_{EZ}$, which we attribute to tunneling events across this barrier between ν_{BG} = 1 and ν_{TG2} = 0 (Fig. 4D).

Note that all nonlocal signals (occurring at ν_{TG2} = −1, 0, and 1) appear only in a finite band of V_{dc}. This suppression of the differential voltage signal indicates that magnon generation is suppressed, or alternatively, that the differently spaced contacts begin to see identical amounts of magnon absorption once the system has reached a certain magnon density threshold. We further speculate that this cutoff could be related to the magnon bandwidth, but we leave this to a future investigation.

The experiments presented here introduce a method of using magnons to probe the SU(4) spin and valley anisotropies of graphene QH systems, which can be used to probe highly correlated states such as the fractional QH regime (*26*) or the quantum spin Hall phase of monolayer graphene (*9*). Owing to the theoretical prediction for spin superfluidity in the CAF state (*12*), this study paves the way for exploring and realizing dissipationless spin waves in a Bose-Einstein condensate (BEC) of magnons. Such condensates should result in a coherent precession of the spins in the QH magnet, which may be probed through emitted microwave radiation. Furthermore, coherent spin waves associated with a BEC may be able to propagate long distances with negligible dissipation, which could be tested by careful length dependence measurements.

REFERENCES AND NOTES

1. S. M. Girvin, in *Topological Aspects of Low Dimensional Systems*, A. Comtet, T. Jolicœur, S. Ouvry, F. David, Eds. (Springer, 2000), pp. 53–175.
2. A. F. Young *et al.*, *Nat. Phys.* **8**, 550–556 (2012).
3. S. L. Sondhi, A. Karlhede, S. A. Kivelson, E. H. Rezayi, *Phys. Rev. B* **47**, 16419–16426 (1993).
4. J. Alicea, M. P. A. Fisher, *Phys. Rev. B* **74**, 075422 (2006).
5. K. Yang, S. Das Sarma, A. H. MacDonald, *Phys. Rev. B* **74**, 075423 (2006).
6. Y. Zhang *et al.*, *Phys. Rev. Lett.* **96**, 136806 (2006).
7. K. Nomura, A. H. MacDonald, *Phys. Rev. Lett.* **96**, 256602 (2006).
8. M. O. Goerbig, *Rev. Mod. Phys.* **83**, 1193–1243 (2011).
9. A. F. Young *et al.*, *Nature* **505**, 528–532 (2014).
10. M. Kharitonov, *Phys. Rev. B* **85**, 155439 (2012).
11. A. G. Green, N. R. Cooper, *Phys. Rev. B* **65**, 125329 (2002).
12. S. Takei, A. Yacoby, B. I. Halperin, Y. Tserkovnyak, *Phys. Rev. Lett.* **116**, 216801 (2016).
13. F. Amet, J. R. Williams, K. Watanabe, T. Taniguchi, D. Goldhaber-Gordon, *Phys. Rev. Lett.* **112**, 196601 (2014).
14. D. S. Wei *et al.*, *Sci. Adv.* **3**, e1700600 (2017).
15. C. Kittel, *Phys. Rev.* **73**, 155–161 (1948).
16. Y. Kajiwara *et al.*, *Nature* **464**, 262–266 (2010).
17. L. J. Cornelissen, J. Liu, R. A. Duine, J. Ben Youssef, B. J. Van Wees, *Nat. Phys.* **11**, 1022–1026 (2015).
18. A. V. Chumak, V. I. Vasyuchka, A. A. Serga, B. Hillebrands, *Nat. Phys.* **11**, 453–461 (2015).
19. D. Wesenberg, T. Liu, D. Balzar, M. Wu, B. L. Zink, *Nat. Phys.* **13**, 987–993 (2017).
20. J. R. Williams, L. Dicarlo, C. M. Marcus, *Science* **317**, 638–641 (2007).
21. B. Özyilmaz *et al.*, *Phys. Rev. Lett.* **99**, 166804 (2007).
22. See supplementary materials.
23. G. Giovannetti *et al.*, *Phys. Rev. Lett.* **101**, 026803 (2008).
24. A. Schmeller, J. P. Eisenstein, L. N. Pfeiffer, K. W. West, *Phys. Rev. Lett.* **75**, 4290–4293 (1995).
25. G. Nachtwei, *Physica E* **4**, 79–101 (1999).
26. A. H. MacDonald, J. J. Palacios, *Phys. Rev. B* **58**, R10171 (1998).

ACKNOWLEDGMENTS

We thank A. H. Macdonald, J. D. Sanchez-Yamagishi, S. L. Tomarken, and S. P. Harvey for helpful discussions and feedback, X. Liu for fabrication help, and P. Kim for providing the transfer setup. **Funding:** Supported by the Gordon and Betty Moore Foundation's EPiQS Initiative through grant GBMF4531; the U.S. Department of Energy, Basic Energy Sciences Office, Division of Materials Sciences and Engineering under award DE-SC0001819 (D.S.W. and T.v.d.S.); NSF Graduate Research Fellowship grant DGE1144152 (D.S.W.); the STC Center for Integrated Quantum Materials, NSF grant DMR-1231319 (B.I.H.); and the Elemental Strategy Initiative conducted by MEXT, Japan, and JSPS KAKENHI grant JP15K21722 (K.W. and T.T.). Nanofabrication was performed at the Center for Nanoscale Systems at Harvard, supported in part by NSF NNIN award ECS-00335765. **Author contributions:** D.S.W., T.v.d.S., B.I.H., and A.Y. conceived and designed the experiments; D.S.W. fabricated the devices; D.S.W. and A.Y. performed the experiments; D.S.W., T.v.d.S., S.H.L., B.I.H., and A.Y. analyzed the data and wrote the paper; and K.W. and T.T. synthesized the hexagonal boron nitride crystals. **Competing interests:** The authors declare no competing financial interests. **Data and materials availability:** All measured data are available in the supplementary materials.

SUPPLEMENTARY MATERIALS

www.sciencemag.org/content/362/6411/229/suppl/DC1
Materials and Methods
Supplementary Text
Figs. S1 to S11
References (*27*–*39*)
Data Files

5 November 2017; accepted 19 August 2018
10.1126/science.aar4061

Science

Electrical generation and detection of spin waves in a quantum Hall ferromagnet

Di S. Wei, Toeno van der Sar, Seung Hwan Lee, Kenji Watanabe, Takashi Taniguchi, Bertrand I. Halperin and Amir Yacoby

Science **362** (6411), 229-233.
DOI: 10.1126/science.aar4061

Magnons propagating in graphene

At sufficiently low temperatures, a two-dimensional electron system placed in an external magnetic field can exhibit the so-called quantum Hall effect. In this regime, a variety of magnetic phases may occur, depending on the electron density and other factors. Wei *et al.* studied the properties of these exotic magnetic phases in graphene. They generated magnons—the excitations of an ordered magnetic system—that were then absorbed by the sample, leaving a mark on its electrical conductance. The magnons were able to propagate across long distances through various magnetic phases in the bulk graphene.

Science, this issue p. 229